Chapter 2
The Tight-Binding Approach and the Resulting Electronic Structure

In this chapter, we describe the crystal and reciprocal lattices of bilayer graphene. We also discuss briefly the symmetry of the crystal lattice. We then introduce the tight-binding model for π electrons in bilayer graphene. We start with a general formulation valid for all points in the Brillouin zone and the resulting electronic structure. Next, we concentrate on the linear approximation of that model around the corners of the Brillouin zone. This tight-binding approach is a variation of the tight-binding model for monolayer graphene as developed historically for applications in the physics of graphite (then so called Slonczewski–Weiss–McClure model [1–4]). For an introduction to the tight-binding approach in carbon sp^2 materials, see Refs. [5] or [6]. In the following section, we introduce symmetry-breaking parameters which will later turn out to be very important when interpreting results of spectroscopic measurements. We conclude the chapter with the derivation of the effective low-energy, two-band Hamiltonian for bilayer graphene.

2.1 The Crystal and Reciprocal Lattices

Bilayer graphene consists of two coupled graphene layers of carbon atoms (graphene monolayers) arranged in Bernal (AB) stacking [7, 8]. The unit cell contains four inequivalent carbon sites $A1$, $B1$, $A2$, and $B2$, where A and B denote two triangular sublattices in the same layer while 1 and 2 distinguish between the bottom and top layer, respectively. The real lattice of bilayer graphene is schematically shown in Fig. 2.1a. The honeycomb lattice of the bottom and top layers has been drawn with red and black solid lines, respectively. The lattice constant a, that is the $A-A$ (or $B-B$) distance, marked in the figure with grey, equals 2.46 Å. This lattice constant derives from the benzene-ring structure and is the same in bilayer graphene as in monolayer graphene or graphite. The interlayer distance, c_0, is much greater than the nearest neighbour carbon-carbon distance $\frac{a}{\sqrt{3}}$ Å. X-ray reflectivity experiments and first-principles calculations performed for bilayer graphene epitaxialy grown on

M. Mucha-Kruczyński, *Theory of Bilayer Graphene Spectroscopy*,
Springer Theses, DOI: 10.1007/978-3-642-30936-6_2,

Table 2.1 Components of the vectors in the real and reciprocal lattices shown in Fig. 2.1 and used throughout the text

vector component	$\boldsymbol{a}_1$	$\boldsymbol{a}_2$	$\boldsymbol{d}_1$	$\boldsymbol{d}_2$	$\boldsymbol{d}_3$	$\boldsymbol{b}_1$	$\boldsymbol{b}_2$	$\boldsymbol{K}_+$	$\boldsymbol{K}_-$
x or k_x	$\frac{a}{2}$	$\frac{a}{2}$	0	$\frac{a}{2}$	$-\frac{a}{2}$	$\frac{2\pi}{a}$	$\frac{2\pi}{a}$	$\frac{4\pi}{3a}$	$-\frac{4\pi}{3a}$
y or k_y	$\frac{a\sqrt{3}}{2}$	$-\frac{a\sqrt{3}}{2}$	$\frac{a}{\sqrt{3}}$	$-\frac{a}{2\sqrt{3}}$	$-\frac{a}{2\sqrt{3}}$	$\frac{2\pi}{a\sqrt{3}}$	$-\frac{2\pi}{a\sqrt{3}}$	0	0

SiC [9], as well as first-principles calculations for bilayer in vacuum [10], lead to $c_o \approx 3.35\,\text{Å}$, as in graphite. We choose vectors $\boldsymbol{a}_1$ and $\boldsymbol{a}_2$ as our in-plane primitive lattice vectors and a rhombic unit cell as shown in Fig. 2.1a with a dashed blue line. Also shown in the figure are vectors $\boldsymbol{d}_1$, $\boldsymbol{d}_2$ and $\boldsymbol{d}_3$, which can be used to express the distance between neighbouring in-plane carbon atoms. Eventually, we use vector $\boldsymbol{c}_0 = (0, 0, c_0)$ to describe the thickness of the bilayer.

The corresponding reciprocal lattice is schematically presented in Fig. 2.1b. It is two-dimensional, because bilayer graphene, although strictly speaking three-dimensional due to the interlayer spacing, is not periodic in the z direction. The reciprocal unit vectors $\boldsymbol{b}_1$ and $\boldsymbol{b}_2$, related to $\boldsymbol{a}_1$ and $\boldsymbol{a}_2$ via the condition $\boldsymbol{b}_i \cdot \boldsymbol{a}_j = 2\pi\delta_{ij}$, are shown in darker blue. The Brillouin zone is a hexagon, marked in the figure with a dashed line. We denote two inequivalent corners of the Brillouin zone (later also called valleys) as K_+ (at the position $\boldsymbol{K}_+ = (4\pi/3a, 0)$) and K_- (at the position $\boldsymbol{K}_- = (-4\pi/3a, 0)$) and reserve index $\xi = \pm$ to distinguish between them in further discussions.

The real primitive lattice vectors $\boldsymbol{a}_1$ and $\boldsymbol{a}_2$, reciprocal primitive vectors $\boldsymbol{b}_1$ and $\boldsymbol{b}_2$, nearest neighbour vectors $\boldsymbol{d}_i$, as well as the coordinates of the valley K_ξ are repeatedly used throughout the remaining parts of the thesis. For convenience, all aforementioned vectors and their components in their respective space have been summarised in Table 2.1.

2.2 The Four-Band Tight-Binding Model for π Electrons

2.2.1 Full Momentum Dependence

Let us consider an infinite sheet of bilayer graphene. For the origin of the coordinate system, we choose the centre of a unit cell (position of the $B1 - A2$ dimer, at the point halfway between the layers) and denote by $\boldsymbol{r}$ and $\boldsymbol{R}_0$ the position vector and a vector pointing to the centre of another unit cell (one of N in total), respectively. We reserve symbol $\boldsymbol{R}_i$ to represent a vector pointing from the centre of a unit cell to the atomic site i (i then stands for $A1$, $B1$, $A2$ or $B2$) in this unit cell. We assume periodic boundary conditions and construct a basis of functions $\phi_{\boldsymbol{k},i}(\boldsymbol{r})$ built up from the π orbitals $\varphi(\mathbf{r})$ of carbon atoms in site i,

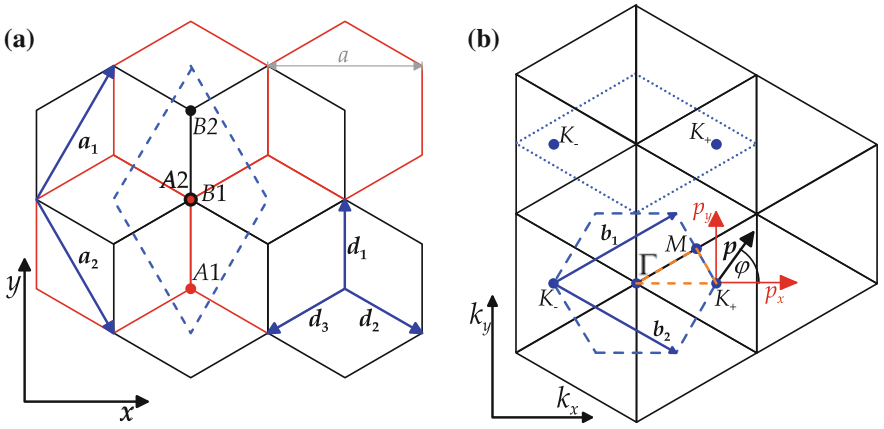

Fig. 2.1 **a** Schematic drawing of the bilayer graphene crystal lattice. The *bottom* (*top*) *layer* is depicted with *red* (*black*) *solid lines*. The real primitive lattice vectors are $\boldsymbol{a}_1$ and $\boldsymbol{a}_2$ and the unit cell is shown with *dashed blue line*. *Grey line* marks the lattice constant a. Vectors $\boldsymbol{d}_1$, $\boldsymbol{d}_2$, and $\boldsymbol{d}_3$, are used to express the relative position of neighbouring carbon atoms. **b** The reciprocal lattice of bilayer graphene with the Brillouin zone shown with the *dashed blue line* and its two inequivalent corners (valleys) K_+ and K_-. In contrast, the dotted blue line shows an alternative, rhombic unit cell in reciprocal space used briefly in Chap. 3. The *orange dashed line* shows the high-symmetry directions for which the band structure in Fig. 2.2 is shown

$$
\begin{aligned}
\phi_{\boldsymbol{k},A1}(\boldsymbol{r}) &= \frac{1}{\sqrt{N}} \sum_{\boldsymbol{R}_0} e^{i\boldsymbol{k}\cdot(\boldsymbol{R}_0 - \boldsymbol{d}_1 - \frac{\boldsymbol{c}_0}{2})} \varphi\big(\boldsymbol{r} - \boldsymbol{R}_0 + \boldsymbol{d}_1 + \frac{\boldsymbol{c}_0}{2}\big), \\
\phi_{\boldsymbol{k},B1}(\boldsymbol{r}) &= \frac{1}{\sqrt{N}} \sum_{\boldsymbol{R}_0} e^{i\boldsymbol{k}\cdot(\boldsymbol{R}_0 - \frac{\boldsymbol{c}_0}{2})} \varphi\big(\boldsymbol{r} - \boldsymbol{R}_0 + \frac{\boldsymbol{c}_0}{2}\big), \\
\phi_{\boldsymbol{k},A2}(\boldsymbol{r}) &= \frac{1}{\sqrt{N}} \sum_{\boldsymbol{R}_0} e^{i\boldsymbol{k}\cdot(\boldsymbol{R}_0 + \frac{\boldsymbol{c}_0}{2})} \varphi\big(\boldsymbol{r} - \boldsymbol{R}_0 - \frac{\boldsymbol{c}_0}{2}\big), \\
\phi_{\boldsymbol{k},B2}(\boldsymbol{r}) &= \frac{1}{\sqrt{N}} \sum_{\boldsymbol{R}_0} e^{i\boldsymbol{k}\cdot(\boldsymbol{R}_0 + \boldsymbol{d}_1 + \frac{\boldsymbol{c}_0}{2})} \varphi\big(\boldsymbol{r} - \boldsymbol{R}_0 - \boldsymbol{d}_1 - \frac{\boldsymbol{c}_0}{2}\big),
\end{aligned}
\tag{2.1}
$$

where $\boldsymbol{k}$ is a two-dimensional electron wave vector.

The electron wave function $\Psi_j(\boldsymbol{r})$, corresponding to the energy eigenvalue $\epsilon_j(\boldsymbol{k})$ of an electron with wave vector $\boldsymbol{k}$, is a linear combination of functions in Eq. (2.1),

$$
\Psi_j(\boldsymbol{r}) = \sum_i C_{ij} \phi_{\boldsymbol{k},i}(\boldsymbol{r}). \tag{2.2}
$$

It is easy to see that $\Psi_j(\boldsymbol{r})$ satisfies Bloch's theorem, as we have

$$
\Psi_j(\boldsymbol{r} + m\boldsymbol{a}_1 + n\boldsymbol{a}_2) = \sum_i C_{ij} \phi_{\boldsymbol{k},i}(\boldsymbol{r} + m\boldsymbol{a}_1 + n\boldsymbol{a}_2) = e^{i\boldsymbol{k}\cdot(m\boldsymbol{a}_1 + n\boldsymbol{a}_2)} \Psi_j(\boldsymbol{r}). \tag{2.3}
$$

By using the variational principle, we arrive with the matrix equation for the column vector ψ_j of the coefficients C_{ij},

$$\hat{\boldsymbol{H}}\psi_j = \epsilon_j(\boldsymbol{k})\hat{\boldsymbol{S}}\psi_j. \tag{2.4}$$

To explicitly write down the form of the Hamiltonian operator $\hat{\boldsymbol{H}}$ and the overlap operator $\hat{\boldsymbol{S}}$, we choose the order of the basis functions from Eq. (2.1) to be

$$\phi_{\boldsymbol{k}}(\boldsymbol{r}) = (\phi_{\boldsymbol{k},A1}(\boldsymbol{r}), \phi_{\boldsymbol{k},B2}(\boldsymbol{r}), \phi_{\boldsymbol{k},A2}(\boldsymbol{r}), \phi_{\boldsymbol{k},B1}(\boldsymbol{r}))^T.$$

We assume that the interaction between two carbon atoms depends only on the distance between them. Also, for a carbon atom on site i, we take into account only its interaction with the closest carbon atoms on sites j. We make an exception for the interaction of an atom on site i with another on site i, where we include the influence of next-nearest neighbour of the same kind. The phase factor resulting from a summation over nearest neighbours can, for any carbon atom, be written in terms of the vectors $\boldsymbol{d}_1$, $\boldsymbol{d}_2$ and $\boldsymbol{d}_3$. We define the geometrical factor $f(\boldsymbol{k})$,

$$f(\boldsymbol{k}) \equiv \sum_{i=1}^{3} e^{i\boldsymbol{k}\cdot\boldsymbol{d}_i} = e^{i\frac{k_y a}{\sqrt{3}}} + 2e^{-i\frac{k_y a}{2\sqrt{3}}}\cos\frac{k_x a}{2}. \tag{2.5}$$

As a result, the full matrix form of the operators $\hat{\boldsymbol{H}}$ and $\hat{\boldsymbol{S}}$ is[1]:

$$\hat{\boldsymbol{H}} = \begin{pmatrix} \epsilon_{A1} - \gamma_n|f(\boldsymbol{k})|^2 & -\gamma_3 f^*(\boldsymbol{k}) & \gamma_4 f(\boldsymbol{k}) & -\gamma_0 f(\boldsymbol{k}) \\ -\gamma_3 f(\boldsymbol{k}) & \epsilon_{B2} - \gamma_n|f(\boldsymbol{k})|^2 & -\gamma_0 f^*(\boldsymbol{k}) & \gamma_4 f^*(\boldsymbol{k}) \\ \gamma_4 f^*(\boldsymbol{k}) & -\gamma_0 f(\boldsymbol{k}) & \epsilon_{A2} - \gamma_n|f(\boldsymbol{k})|^2 & \gamma_1 \\ -\gamma_0 f^*(\boldsymbol{k}) & \gamma_4 f(\boldsymbol{k}) & \gamma_1 & \epsilon_{B1} - \gamma_n|f(\boldsymbol{k})|^2 \end{pmatrix}; \tag{2.6a}$$

$$\hat{\boldsymbol{S}} = \begin{pmatrix} 1 & 0 & 0 & s_0 f(\boldsymbol{k}) \\ 0 & 1 & s_0 f^*(\boldsymbol{k}) & 0 \\ 0 & s_0 f(\boldsymbol{k}) & 1 & s_1 \\ s_0 f^*(\boldsymbol{k}) & 0 & s_1 & 1 \end{pmatrix}. \tag{2.6b}$$

In the above, we introduced several parameters into the model as a description of the strength of interactions between carbon atoms. In this, we mostly follow the Slonczewski-Weiss-McClure model developed for bulk graphite [1–4] (for a review see Ref. [8]). The on-site energies ϵ_i, couplings γ_j and overlap parameters s_l used in Eq. (2.6) are given by:

[1] We neglect in Eq. (2.6a) a factor of $3\gamma_n$ appearing on the diagonal as it only leads to a shift of zero on the energy scale.

$$\epsilon_i \equiv \langle \varphi(\boldsymbol{r} - \boldsymbol{R}_0 - \boldsymbol{R}_i)|\hat{\boldsymbol{H}}|\varphi(\boldsymbol{r} - \boldsymbol{R}_0 - \boldsymbol{R}_i)\rangle, \tag{2.7a}$$

$$\begin{aligned}\gamma_0 &\equiv -\langle \varphi(\boldsymbol{r} - \boldsymbol{R}_0 - \boldsymbol{R}_{A1})|\hat{\boldsymbol{H}}|\varphi(\boldsymbol{r} - \boldsymbol{R}_0 - \boldsymbol{R}_{A1} - \boldsymbol{d}_i)\rangle \\ &\equiv -\langle \varphi(\boldsymbol{r} - \boldsymbol{R}_0 - \boldsymbol{R}_{A2})|\hat{\boldsymbol{H}}|\varphi(\boldsymbol{r} - \boldsymbol{R}_0 - \boldsymbol{R}_{A2} - \boldsymbol{d}_i)\rangle,\end{aligned} \tag{2.7b}$$

$$\gamma_1 \equiv \langle \varphi(\boldsymbol{r} - \boldsymbol{R}_0 - \boldsymbol{R}_{B1})|\hat{\boldsymbol{H}}|\varphi(\boldsymbol{r} - \boldsymbol{R}_0 - \boldsymbol{R}_{A2})\rangle, \tag{2.7c}$$

$$\gamma_3 \equiv -\langle \varphi(\boldsymbol{r} - \boldsymbol{R}_0 - \boldsymbol{R}_{A1})|\hat{\boldsymbol{H}}|\varphi(\boldsymbol{r} - \boldsymbol{R}_0 - \boldsymbol{R}_{A1} + \boldsymbol{d}_i - \boldsymbol{c}_0)\rangle, \tag{2.7d}$$

$$\begin{aligned}\gamma_4 &\equiv \langle \varphi(\boldsymbol{r} - \boldsymbol{R}_0 - \boldsymbol{R}_{A1})|\hat{\boldsymbol{H}}|\varphi(\boldsymbol{r} - \boldsymbol{R}_0 - \boldsymbol{R}_{A1} - \boldsymbol{d}_1 - \boldsymbol{c}_0)\rangle \\ &\equiv \langle \varphi(\boldsymbol{r} - \boldsymbol{R}_0 - \boldsymbol{R}_{B1})|\hat{\boldsymbol{H}}|\varphi(\boldsymbol{r} - \boldsymbol{R}_0 - \boldsymbol{R}_{B1} - \boldsymbol{d}_1 - \boldsymbol{c}_0)\rangle,\end{aligned} \tag{2.7e}$$

$$\gamma_n \equiv \langle \varphi(\boldsymbol{r} - \boldsymbol{R}_0 - \boldsymbol{R}_i)|\hat{\boldsymbol{H}}|\varphi(\boldsymbol{r} - \boldsymbol{R}_0 - \boldsymbol{R}_i + \boldsymbol{d}_3 - \boldsymbol{d}_2)\rangle, \tag{2.7f}$$

$$\begin{aligned}s_0 &\equiv \langle \varphi(\boldsymbol{r} - \boldsymbol{R}_0 - \boldsymbol{R}_{A1})|\varphi(\boldsymbol{r} - \boldsymbol{R}_0 - \boldsymbol{R}_{A1} - \boldsymbol{d}_i)\rangle \\ &\equiv \langle \varphi(\boldsymbol{r} - \boldsymbol{R}_0 - \boldsymbol{R}_{A2})|\varphi(\boldsymbol{r} - \boldsymbol{R}_0 - \boldsymbol{R}_{A2} - \boldsymbol{d}_i)\rangle,\end{aligned} \tag{2.7g}$$

$$s_1 \equiv \langle \varphi(\boldsymbol{r} - \boldsymbol{R}_0 - \boldsymbol{R}_{B1})|\varphi(\boldsymbol{r} - \boldsymbol{R}_0 - \boldsymbol{R}_{A2})\rangle. \tag{2.7h}$$

The diagonal terms ϵ_i denote the on-site energy of the electron at the carbon atom in site i. In the first approximation, they are equal to the energy of an electron in the $2p_z$ orbital of a carbon atom. This energy is modified as carbon atoms bond together to form the lattice. However, in an ideal and charge-neutral bilayer, this on-site energy is approximately the same for each site in the lattice. In this case, we can take it to be zero and define our energy scale relatively to this point. More complicated situations in which the symmetry between the atomic sites has been broken are discussed in Sect. 2.2.3.

The parameters γ_j describe the strength of the coupling between a specific pair of carbon atoms. The constant γ_0 denotes the coupling between the nearest neighbours ($A1 \leftrightarrow B1$ and $A2 \leftrightarrow B2$). The parameter γ_1 describes the direct interlayer coupling $A2 \leftrightarrow B1$. The γ_3 coupling represents the interlayer interaction between the nearest $A1$ and $B2$ atoms, whereas γ_4 characterizes the interlayer coupling between the nearest $A1$ and $A2$, as well as $B1$ and $B2$ atoms. Naively, one could expect the couplings γ_3 and γ_4 to be equal, especially with the assumptions made above about couplings dependent only on the interatomic distance. However, with some insight from the Slonczewski–Weiss–McClure model, we allow for γ_3 and γ_4 to be different. Physically, this is the case because, as opposed to γ_3, γ_4 involves one of the atomic sites creating the "dimer" ($B1$ and $A2$). The last coupling, γ_n, describes the interaction of the in-plane next-nearest neighbours.

The overlap integrals s_l take into account the fact that our π orbitals do not span an orthogonal basis set. We only included here the overlap s_0 between two nearest neighbour atoms and the overlap s_1 between the $A2$ and $B1$ sites where atoms are directly above/below each other. Due to their small value, in most of the situations under consideration in this thesis, even these two overlap integrals are neglected.

The electronic band structure resulting from Eq. (2.4) with the Hamiltonian and overlap matrices $\hat{\boldsymbol{H}}$ and $\hat{\boldsymbol{S}}$ as in Eq. (2.6) is shown in Fig. 2.2. We see two conduction and two valence bands. The lower conduction band and the upper valence band touch

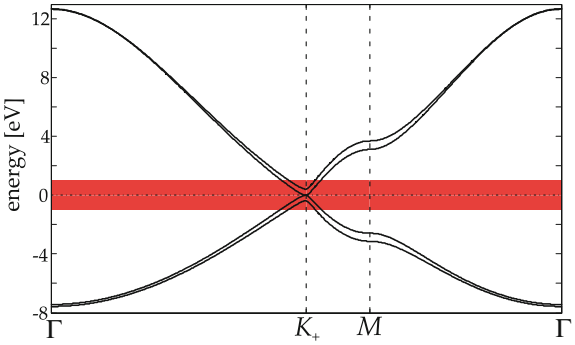

Fig. 2.2 The band structure of bilayer graphene resulting from Eq. (2.4) with the Hamiltonian and overlap matrices $\hat{\boldsymbol{H}}$ and $\hat{\boldsymbol{S}}$ as in Eq. (2.6) presented for high-symmetry directions in the Brillouin zone as shown in Fig. 2.1b. The values of the parameters used are: $\gamma_0 = 3.1\,\text{eV}$, $\gamma_1 = 0.4\,\text{eV}$, $\gamma_3 = 0.15\,\text{eV}$, $\gamma_4 = 0.1\,\text{eV}$, $\gamma_n = 0.05\,\text{eV}$, $s_0 = 0.1$, $s_1 = -0.05$, $\epsilon_i = 0$ for all i, and $a = 2.46\,\text{Å}$. The range of energies important in experimental setups modelled theoretically in this work is shown on *red* background

exactly at the K point. The position of this touching point at the energy scale denotes half-filling of the bands and is called the neutrality point. It is usually treated as the zero of the energy scale. In the neutral structure with the valence bands completely filled, the Fermi surface consists only of points. Any shift of the chemical potential results in the creation of separate Fermi lines around each of the K points. Due to this behaviour of the Fermi surface, the K points are often refered to as *valleys*. We point out that for most experiments and potential applications, only the part of the dispersion relatively close to the neutrality point ($\sim$1 eV) is important and interesting. Indeed, a proper description of this part of the band structure forms the basis for the understanding and theoretical modelling of spectroscopic experiments presented in this thesis. We will, therefore, investigate it in more detail in the following sections.

2.2.2 Approximation for Hopping Elements

We now want to look closer at the electronic dispersion for energies relevant to most experiments, that is, the energies of up to $\sim$1 eV from the neutrality point. This range of energies is marked with red background in Fig. 2.2. For such energy, the relevant regions in momentum space are the vicinities of the six corners of the Brillouin zone. To describe electronic dispersion around a local minima at the K points, we shift the coordinate system in reciprocal (momentum) space from the Γ point to the K_ξ point. We write the electron wave vector as $\boldsymbol{k} = \boldsymbol{K}_\xi + \frac{\boldsymbol{p}}{\hbar}$, where the electronic momentum $\boldsymbol{p}$ is now measured from the centre of the valley K_ξ. The geometrical factor $f(\boldsymbol{k})$ from Eq. (2.5), expanded up to the second order in $\boldsymbol{p}$, reads

$$f(\boldsymbol{k}) \approx -\frac{\sqrt{3}a}{2\hbar}\left(\xi p_x - i p_y\right) + \frac{a^2}{8\hbar^2}\left(p_x + i p_y\right)^2 . \tag{2.8}$$

We introduce some new parameters, namely velocities $v = \frac{\sqrt{3}a\gamma_0}{2\hbar}$, $v_3 = \frac{\sqrt{3}a\gamma_3}{2\hbar}$ and $v_4 = -\frac{\sqrt{3}a\gamma_4}{2\hbar}$, constant $\eta = \frac{a^2\gamma_0}{8\hbar^2} \equiv \frac{v^2}{6\gamma_0}$, as well as operators, $\hat{\boldsymbol{\pi}} = p_x + ip_y$ and $\hat{\boldsymbol{\pi}}^\dagger = p_x - ip_y$. We also neglect at this stage the overlap integrals s_0 and s_1, and hence obtain only a unit matrix on the right hand side of Eq. (2.4). Our basis now consists of 8 functions $\phi_{\boldsymbol{p},\xi,i}(\boldsymbol{r})$ (4 for each valley). However, for the cases considered in this thesis, the valleys can be regarded as independent (we do not consider any valley-connecting processes) and it is usually enough to explicitly write down only the electronic Hamiltonian $\hat{\boldsymbol{H}}_\xi$ for one valley K_ξ,

$$\hat{\boldsymbol{H}}_\xi = \xi \begin{pmatrix} 0 & v_3\hat{\boldsymbol{\pi}} & v_4\hat{\boldsymbol{\pi}}^\dagger & v\hat{\boldsymbol{\pi}}^\dagger \\ v_3\hat{\boldsymbol{\pi}}^\dagger & 0 & v\hat{\boldsymbol{\pi}} & v_4\hat{\boldsymbol{\pi}} \\ v_4\hat{\boldsymbol{\pi}} & v\hat{\boldsymbol{\pi}}^\dagger & 0 & \xi\gamma_1 \\ v\hat{\boldsymbol{\pi}} & v_4\hat{\boldsymbol{\pi}}^\dagger & \xi\gamma_1 & 0 \end{pmatrix} - \eta \begin{pmatrix} \frac{6\gamma_n}{\gamma_0}p^2 & \frac{v_3}{v}(\hat{\boldsymbol{\pi}}^\dagger)^2 & \frac{v_4}{v}\hat{\boldsymbol{\pi}}^2 & \hat{\boldsymbol{\pi}}^2 \\ \frac{v_3}{v}\hat{\boldsymbol{\pi}}^2 & \frac{6\gamma_n}{\gamma_0}p^2 & (\hat{\boldsymbol{\pi}}^\dagger)^2 & \frac{v_4}{v}(\hat{\boldsymbol{\pi}}^\dagger)^2 \\ \frac{v_4}{v}(\hat{\boldsymbol{\pi}}^\dagger)^2 & \hat{\boldsymbol{\pi}}^2 & \frac{6\gamma_n}{\gamma_0}p^2 & 0 \\ (\hat{\boldsymbol{\pi}}^\dagger)^2 & \frac{v_4}{v}\hat{\boldsymbol{\pi}}^2 & 0 & \frac{6\gamma_n}{\gamma_0}p^2 \end{pmatrix}. \tag{2.9}$$

In the Hamiltonian above, we have for now neglected the on-site energies ϵ_i, which are discussed in detail in Sect. 2.2.3. The order of the basis functions is[2] $(\phi_{+,A1}, \phi_{+,B2}, \phi_{+,A2}, \phi_{+,B1})^T$ in the K_+ and $(\phi_{-,B2}, \phi_{-,A1}, \phi_{-,B1}, \phi_{-,A2})^T$ in the K_- valley.

The same Hamiltonian can be obtained using the '$\mathbf{k}\cdot\mathbf{p}$' approximation (see for example [11, 12] for detailed derivation). In this scheme, as a basis set we use functions $\tilde{\phi}_{\boldsymbol{p},\xi,i}(\boldsymbol{r})$ constructed from $\phi_{\boldsymbol{k},i}(\boldsymbol{r})$, Eq. (2.1), calculated exactly in the centre of the valley K_ξ and a plane wave envelope function which varies slowly at the distance of the order of the lattice constant a [13, 14]:

$$\tilde{\phi}_{\boldsymbol{p},\xi,i}(\boldsymbol{r}) \equiv e^{\frac{i}{\hbar}\boldsymbol{p}\cdot\boldsymbol{r}}\phi_{\boldsymbol{K}_\xi,i}(\boldsymbol{r}) \equiv \frac{1}{\sqrt{N}}e^{\frac{i}{\hbar}\boldsymbol{p}\cdot\boldsymbol{r}}\sum_{\boldsymbol{R}_0} e^{i\boldsymbol{K}_\xi\cdot(\boldsymbol{R}_0+\boldsymbol{R}_i)}\varphi\big(\boldsymbol{r}-\boldsymbol{R}_0-\boldsymbol{R}_i\big).$$

Comparing functions $\tilde{\phi}_{\boldsymbol{p},\xi,i}(\boldsymbol{r})$ and $\phi_{\boldsymbol{K}_\xi+\frac{\boldsymbol{p}}{\hbar},i}(\boldsymbol{r})$, we can intuitively see why the Hamiltonians in both approximations take the same form. Both functions take similar values for $\boldsymbol{r} \approx \boldsymbol{R}_0 - \boldsymbol{R}_i$, whereas in other regions the π orbital $\varphi(\boldsymbol{r}-\boldsymbol{R}_0-\boldsymbol{R}_i)$ ensures that they both quickly decay, rendering the phase factors unimportant.

The electronic band structure resulting from the Hamiltonian (2.9) is shown for both valleys in Fig. 2.3 for the energy range $3.5\gamma_1$ away from the neutrality point. On this scale, all bands look approximately parabolic very close to the center of the valley and linear further away. The former is not exactly true for the bands shown in yellow (later referred to as the low-energy bands), as shown in Sect. 2.3. The bands marked in red (in what follows called the high-energy or split bands) are shifted away from the neutrality point by approximately the interlayer coupling, $\gamma_1 \sim 0.4\,\mathrm{eV}$ [15–23] in each direction. The velocity $v \sim 10^6\,\mathrm{m/s}$ [18–20, 23] determines the slope of the

[2] For brevity, we omit the momentum index $\boldsymbol{p}$ and explicit dependence of the basis functions $\phi_{\boldsymbol{p},\xi,i}$ on $\boldsymbol{r}$.

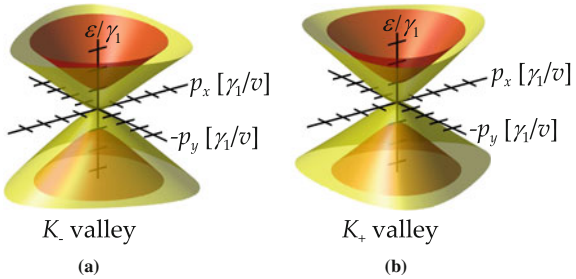

Fig. 2.3 The band structure of bilayer graphene in the vicinity of both (**a**) K_- and (**b**) K_+ valleys, obtained within the linear approximation, Eq. (2.9). The values of the parameters used are: $\gamma_0 = 3.1\,\text{eV}$, $\gamma_1 = 0.4\,\text{eV}$, $\gamma_3 = 0.2\,\text{eV}$, $\gamma_4 = 0.1\,\text{eV}$, $\gamma_n = 0.1\,\text{eV}$, $a = 2.46\,\text{Å}$. No on-site asymmetries are included (that is, $\epsilon_i = 0$ for all i). For both valleys, the low-energy and high-energy bands are shown in *yellow* and *red*, respectively

linear parts of the bands. The isoenergetic lines create circles, which in the case of the low-energy bands are trigonally warped. This warping is the effect of the velocity $v_3 \sim 0.1v$ [20, 23] as well as terms quadratic in the momentum $\boldsymbol{p}$. The remaining velocity, v_4, breaks the electron-hole symmetry. It renormalizes somewhat the slopes of the linear parts and its effect is opposite in the conduction and valence bands. The next-nearest neighbour coupling γ_n also breaks the electron-hole symmetry. The parameters v, γ_1 and v_3 are the most important in the description of the electronic dispersion around the valleys. At low energies, the deviation from the electron-hole symmetric situation is negligible for most cases. Also, it is difficult to experimentally separate the contributions of γ_4, γ_n or even s_0 to the electron-hole asymmetry.

2.2.3 Symmetry-Breaking Asymmetries in the on-Site Energies

Up to this point, we considered the kinetic energies of electrons on different atomic sites (the terms ϵ_i in Eq. 2.7a) to be equal. In other words, all the carbon atoms in the lattice were chemically equivalent. However, that is obviously not the case as the environment of the dimer atoms, $B1$ and $A2$, is definitely different than the surroundings of the atoms $A1$ and $B2$. In general, three parameters are needed to account for differences between our four atomic sites. The (not unique) definitions we use here are:

$$\Delta_{AB} = \frac{1}{2}[(\epsilon_{A1} + \epsilon_{A2}) - (\epsilon_{B1} + \epsilon_{B2})]; \tag{2.10a}$$

$$\Delta = \frac{1}{2}[(\epsilon_{A1} + \epsilon_{B2}) - (\epsilon_{B1} + \epsilon_{A2})]; \tag{2.10b}$$

$$u = \frac{1}{2}[(\epsilon_{A1} + \epsilon_{B1}) - (\epsilon_{A2} + \epsilon_{B2})]; \tag{2.10c}$$

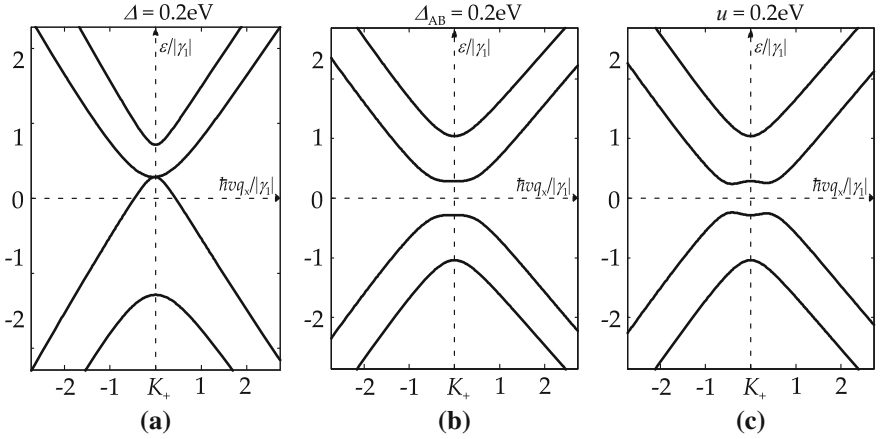

Fig. 2.4 Cuts through the electronic dispersion around the K_+ valley along the p_x axis in the presence of (**a**) $\Delta = 0.2\,\text{eV}$, (**b**) $\Delta_{AB} = 0.2\,\text{eV}$, (**c**) $u = 0.2\,\text{eV}$. For illustrative purposes, we use large values of asymmetries. In reality, only the interlayer asymmetry u can be of the order of 100 meV [25, 26]. The values of other parameters used are: $\gamma_0 = 3\,\text{eV}$, $\gamma_1 = 0.35\,\text{eV}$, $\gamma_3 = 0.15\,\text{eV}$, γ_4, $\gamma_n = 0\,\text{eV}$, $a = 2.46\,\text{Å}$. Figure reprinted from Ref. [27], Copyright (2010), with permission from IOP Publishing

$$\epsilon_{A1} = \frac{1}{2}(u + \Delta + \Delta_{AB}); \qquad \epsilon_{B1} = \frac{1}{2}(u - \Delta - \Delta_{AB}); \tag{2.10d}$$

$$\epsilon_{A2} = \frac{1}{2}(-u - \Delta + \Delta_{AB}); \qquad \epsilon_{B2} = \frac{1}{2}(-u + \Delta - \Delta_{AB}); \tag{2.10e}$$

Then, Δ_{AB} describes the difference between on-site energies of A and B sublattice sites on each layer. We call it intralayer asymmetry. It may be influenced, especially in the bottom layer, by the underlying substrate. The next parameter, Δ, accounts for an energy difference between dimer and non-dimer sites. Finally, u characterizes the interlayer asymmetry between the two layers. This asymmetry can be significantly changed by doping the sample [15] or even continously varied with external gates [24]. This effect is discussed in more depth in Sect. 4.3.1. To show the influence of each of the asymmetries on the band structure, we add them separately to the tight-binding model and plot in Fig. 2.4 cuts through the electronic dispersion around the K_+ point along the p_x axis. The intralayer asymmetry does not open any gaps in the electronic spectrum but breaks the electron-hole symmetry. The dimer/non-dimer asymmetry Δ_{AB} opens a gap and preserves the electron-hole symmetry. The interlayer asymmetry u preserves the electron-hole symmetry and also leads to the opening of a gap in the spectrum. However, we point out the characteristic 'Mexican-hat-like' features in the shape of the low-energy bands in the vicinity of the gap which appear due to u (Fig. 2.4c).

2.3 The Effective Two-Band Model

In this section, we derive an effective low-energy Hamiltonian describing the two degenerate bands in the close vicinity of the valley K_ξ. This analysis was first performed by McCann and Fal'ko [28] and proved extremely useful in describing the low-energy properties of bilayer graphene (see for example Refs. [28–33]). For a detailed discussion of this effective two-band approximation, see Refs. [27, 34]. For simplicity, we take as the starting point the eigenproblem for the Hamiltonian in linear approximation, Eq. (2.9), containing only the most important parameters v, γ_1 and v_3, and terms up to linear in the momentum $\boldsymbol{p}$. We also introduce the Pauli matrices σ_x, σ_y and σ_z, and write the eigenproblem for the Hamiltonian as

$$\begin{pmatrix} \xi v_3(\sigma_x p_x - \sigma_y p_y) & \xi v(\boldsymbol{\sigma}\cdot\boldsymbol{p}) \\ \xi v(\boldsymbol{\sigma}\cdot\boldsymbol{p}) & \sigma_x\gamma_1 \end{pmatrix} \begin{pmatrix} \psi_1 \\ \psi_2 \end{pmatrix} = \epsilon \begin{pmatrix} \psi_1 \\ \psi_2 \end{pmatrix}, \tag{2.11}$$

where ψ_1 and ψ_2 denote two-component vectors which form together the four-component electronic eigenstate ψ_j from (2.4). Let us use the second row of (2.11) to express ψ_2 in terms of ψ_1 and ϵ and substitute it into the first row to obtain,

$$\xi v_3 \left(\sigma_x p_x - \sigma_y p_y\right) \psi_1 + v^2 \left(\boldsymbol{\sigma}\cdot\boldsymbol{p}\right) \left[\epsilon - \sigma_x\gamma_1\right]^{-1} \left(\boldsymbol{\sigma}\cdot\boldsymbol{p}\right) \psi_1 = \epsilon\psi_1.$$

For low energies, $\epsilon \ll \gamma_1$, we get $\left[\epsilon - \sigma_x\gamma_1\right]^{-1} \approx -\frac{\sigma_x}{\gamma_1}$ and

$$\begin{aligned} &\left\{ -\frac{v^2}{\gamma_1} \left[\sigma_x \left(p_x^2 - p_y^2\right) + 2\sigma_y p_x p_y\right] + \xi v_3 \left(\sigma_x p_x - \sigma_y p_y\right) \right\} \psi_1 \\ &\quad \equiv \hat{\boldsymbol{H}}_{\text{eff}} \psi_1 = \epsilon\psi_1. \end{aligned} \tag{2.12}$$

The above effective Hamiltonian describes the electronic dispersion for energies close to the neutrality point while neglecting the split bands. The basis of $\hat{\boldsymbol{H}}_{\text{eff}}$ is $(\phi_{+,A1}, \phi_{+,B2})^T$ at the K_+ and $(\phi_{-,B2}, \phi_{-,A1})^T$ at the K_- valley. The resulting electronic dispersion,

$$\epsilon_\xi = \pm \left[\left(\frac{v^2}{\gamma_1}\right)^2 p^4 + v_3^2 p^2 - \frac{2\xi v^2 v_3}{\gamma_1} p^3 \cos 3\varphi \right]^{\frac{1}{2}}, \tag{2.13}$$

where $p^2 = p_x^2 + p_y^2$ and $\arctan\varphi = \frac{p_y}{p_x}$, is shown in Fig. 2.5a. The trigonally warped isoenergetic line undergoes a splitting into four pockets at the energy $\epsilon_{\text{LT}} = \pm\frac{\gamma_1}{4}\left(\frac{v_3}{v}\right)^2$, $|\epsilon_{\text{LT}}| \sim 1\,\text{meV}$ (a so called Lifshitz transition [35]), see Fig. 2.5b. However, characteristic values for this transition energy ϵ_{LT} and momentum $p_{\text{LT}} \sim \frac{\gamma_1 v_3}{v^2}$ are below the resolution of any of spectroscopies considered in the following chapters. Hence, the only importance of v_3 for our considerations is its role as the main source of trigonal warping for the isoenergetic lines at low energies.

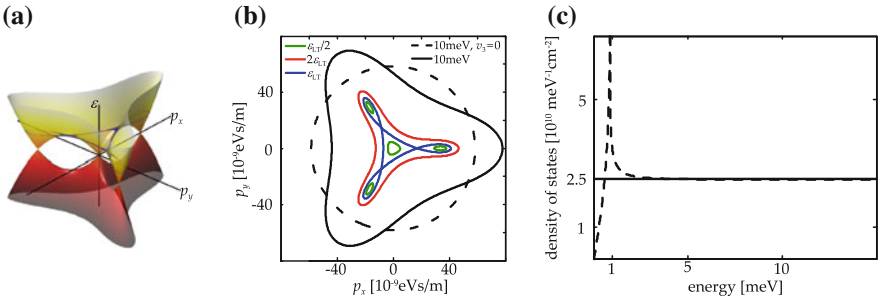

Fig. 2.5 **a** The electronic dispersion of bilayer graphene at very low energies $\epsilon \sim 1\,\text{meV}$ around the valley K_+. The blue contour represents the isoenergetic line at the Lifshitz transition energy $\epsilon_{\text{LT}} = \pm\frac{\gamma_1}{4}\left(\frac{v_3}{v}\right)^2$. **b** The isoenergetic lines around the valley K_+ for energies $\epsilon_{\text{LT}}/2$ (*green solid line*), ϵ_{LT} (*blue solid line*) and $2\epsilon_{\text{LT}}$ (*red solid line*). Also shown are the isoenergetic line at the energy 10 meV from the neutrality point (black solid line) and its shape if the trigonal warping due to v_3 is neglected (*black dashed line*). **c** The density of states given by Eq. (2.13) for $v_3 = 0.1v$ (*dashed line*) and $v_3 = 0$ (*solid line*). The latter corresponds to a purely parabolic bottom of the band

For these energies, trigonal warping does not significantly affect the density of states (DOS), as shown in Fig. 2.5c, where the comparison between the density of states of a purely parabolic band in the case of $v_3 = 0$ (black solid line) and of the electronic dispersion given by Eq. (2.13) (black dashed line), is shown. The peak in the DOS corresponds to the Lifshitz transition. However, for energies $\epsilon > 5\,\text{meV}$ the density of states already closely follows constant density of states for a parabolic band, although the isoenergetic lines may still be significantly noncircular (Fig. 2.5b).

The procedure applied above to obtain the low-energy description of electrons can be easily generalised to include all other terms appearing in the four-band Hamiltonian in linear approximation, Eq. (2.9), as well as the on-site asymmetries from Sect. 2.2.3. We then obtain [27]

$$\hat{\boldsymbol{H}}_{\text{eff}} = \hat{\boldsymbol{H}}_0 + \hat{\boldsymbol{h}}_w + \hat{\boldsymbol{h}}_4 + \hat{\boldsymbol{h}}_n + \hat{\boldsymbol{h}}_u + \hat{\boldsymbol{h}}_\Delta + \hat{\boldsymbol{h}}_{AB}, \tag{2.14a}$$

where

$$\hat{\boldsymbol{H}}_0 = -\frac{v^2}{\gamma_1}\left[\sigma_x\left(p_x^2 - p_y^2\right) + 2\sigma_y p_x p_y\right]; \tag{2.14b}$$

$$\hat{\boldsymbol{h}}_w = \xi v_3\left(\sigma_x p_x - \sigma_y p_y\right) - \eta\frac{v_3}{v}\left[\sigma_x\left(p_x^2 - p_y^2\right) + 2\sigma_y p_x p_y\right]; \tag{2.14c}$$

$$\hat{\boldsymbol{h}}_4 = 2\frac{\gamma_4 v^2}{\gamma_0\gamma_1}p^2; \tag{2.14d}$$

$$\hat{\boldsymbol{h}}_n = -\frac{\gamma_n v^2}{\gamma_0^2}p^2; \tag{2.14e}$$

$$\hat{\boldsymbol{h}}_u = \xi u \left(\frac{1}{2} - \frac{v^2}{\gamma_1^2} p^2 \right) \sigma_z; \tag{2.14f}$$

$$\hat{\boldsymbol{h}}_\Delta = \Delta \left(\frac{1}{2} - \frac{v^2}{\gamma_1^2} p^2 \right); \tag{2.14g}$$

$$\hat{\boldsymbol{h}}_{AB} = \xi \frac{\Delta_{AB}}{2} \sigma_z. \tag{2.14h}$$

References

1. P.R. Wallace, The band theory of graphite. Phys. Rev. **71**, 622 (1947)
2. J.W. McClure, Band structure of graphite and de Haas-van Alphen effect. Phys. Rev. **108**, 612 (1957)
3. J.C. Slonczewski, P.R. Weiss, Band structure of graphite. Phys. Rev. **109**, 272 (1958)
4. J.W. McClure, Theory of diamagnetism of graphite. Phys. Rev. **119**, 606 (1960)
5. R. Saito, G. Dresselhaus, M.S. Dresselhaus, *Physical Properties of Carbon Nanotubes* (Imperial College Press, London, 1998)
6. C. Bena, G. Montambaux, Remarks on the tight-binding model of graphene. New J. Phys. **11**, 095003 (2009)
7. J.D. Bernal, The structure of graphite. Proc. R. Soc. A **106**, 749 (1924)
8. M.S. Dresselhaus, G. Dresselhaus, Intercalation compounds of graphite. Adv. Phys. **30**, 139 (1981)
9. F. Varchon, R. Feng, J. Hass, X. Li, B. Ngoc Nguyen, C. Naud, P. Mallet, J.-Y. Veuillen, C. Berger, E.H. Conrad, L. Magaud, Electronic structure of epitaxial graphene layers on SiC: effect of the substrate. Phys. Rev. Lett. **99**, 126805 (2007)
10. S.B. Trickey, F. Müller-Plathe, G.H.F. Diercksen, Interplanar binding and lattice relaxation in a graphite dilayer. Phys. Rev. B **45**, 4460 (1992)
11. H. Ajiki, T. Ando, Electronic states of carbon nanotubes. J. Phys. Soc. Jpn. **62**, 1255 (1993)
12. T. Ando, Theory of electronic states and transport in carbon nanotubes. J. Phys. Soc. Jpn. **74**, 777 (2005)
13. J.M. Luttinger, W. Kohn, Motion of electrons and holes in perturbed periodic fields. Phys. Rev. **97**, 869 (1955)
14. D.P. DiVincenzo, E.J. Mele, Self-consistent effective-mass theory for intralayer screening in graphite intercalation compounds. Phys. Rev. B **29**, 1685 (1984)
15. T. Ohta, A. Bostwick, T. Seyller, K. Horn, E. Rotenberg, Controlling the electronic structure of bilayer graphene. Science **313**, 951 (2006)
16. L.M. Zhang, Z.Q. Li, D.N. Basov, M.M. Fogler, Z. Hao, M.C. Martin, Determination of the electronic structure of bilayer graphene from infrared spectroscopy. Phys. Rev. B **78**, 235408 (2008)
17. A.B. Kuzmenko, E. van Heumen, D. van der Marel, P. Lerch, P. Blake, K.S. Novoselov, A.K. Geim, Infrared spectroscopy of electronic bands in bilayer graphene. Phys. Rev. B **79**, 115441 (2009)
18. A.B. Kuzmenko, I. Crassee, D. van der Marel, P. Blake, K.S. Novoselov, Determination of the gate-tunable band gap and tight-binding parameters in bilayer graphene using infrared spectroscopy. Phys. Rev. B **80**, 165406 (2009)
19. Z.Q. Li, E.A. Henriksen, Z. Jiang, Z. Hao, M.C. Martin, P. Kim, H.L. Stormer, D.N. Basov, Band structure asymmetry of bilayer graphene revealed by infrared spectroscopy. Phys. Rev. Lett. **102**, 037403 (2009)

20. L.M. Malard, J. Nilsson, D.C. Elias, J.C. Brant, F. Plentz, E.S. Alves, A.H. Castro Neto, M.A. Pimenta, Probing the electronic structure of bilayer graphene by Raman scattering. Phys. Rev. B **76**, 201401(R) (2007)
21. J. Yan, E.A. Henriksen, P. Kim, A. Pinczuk, Observation of anomalous phonon softening in bilayer graphene. Phys. Rev. Lett. **101**, 136804 (2008)
22. A. Das, B. Chakraborty, S. Piscanec, S. Pisana, A.K. Sood, A.C. Ferrari, Phonon renormalization in doped bilayer graphene. Phys. Rev. B **79**, 155417 (2009)
23. D.L. Mafra, L.M. Malard, S.K. Doorn, H. Htoon, J. Nilsson, A.H. Castro Neto, M.A. Pimenta, Observation of the Kohn anomaly near the K point of bilayer graphene. Phys. Rev. B **80**, 241414(R) (2009)
24. J.B. Oostinga, H.B. Heersche, X.L. Liu, A.F. Morpurgo, L.M.K. Vandersypen, Gate-induced insulating state in bilayer graphene devices. Nat. Mater. **7**, 151 (2008)
25. Y. Zhang, T.-T. Tang, C. Girit, Z. Hao, M.C. Martin, A. Zettl, M.F. Crommie, Y.R. Shen, F. Wang, Direct observation of a widely tunable bandgap in bilayer graphene. Nature **459**, 820 (2009)
26. K.F. Mak, C.H. Lui, J. Shan, T.F. Heinz, Observation of an electric-field-induced band gap in bilayer graphene by infrared spectroscopy. Phys. Rev. Lett. **102**, 256405 (2009)
27. M. Mucha-Kruczyński, E. McCann, V.I. Fal'ko, Electron-hole asymmetry and energy gaps in bilayer graphene. Semicond. Sci. Technol. **25**, 033001 (2010)
28. E. McCann, V.I. Fal'ko, Landau level degeneracy and quantum hall effect in a graphite bilayer. Phys. Rev. Lett. **96**, 086805 (2006)
29. D.S.L. Abergel, V.I. Fal'ko, Optical and magneto-optical far-infrared properties of bilayer graphene. Phys. Rev. B **75**, 155430 (2007)
30. M.I. Katsnelson, K.S. Novoselov, A.K. Geim, Chiral tunnelling and the Klein paradox in graphene. Nat. Phys. **2**, 620 (2006)
31. K. Kechedzhi, E. McCann, V. Fal'ko, B. Altshuler, Influence of trigonal warping on interference effects in bilayer graphene. Phys. Rev. Lett. **98**, 176806 (2007)
32. K.S. Novoselov, E. McCann, S.V. Morozov, V.I. Fal'ko, M.I. Katsnelson, U. Zeitler, D. Jiang, F. Schedin, A.K. Geim, Unconventional quantum Hall effect and Berry's phase of 2pi in bilayer graphene. Nat. Phys. **2**, 177 (2006)
33. M.I. Katsnelson, Minimal conductivity in bilayer graphene. Eur. Phys. J. B **52**, 151 (2006)
34. E. McCann, D.S.L. Abergel, V.I. Fal'ko, Electrons in bilayer graphene. Solid State Commun. **143**, 110 (2007)
35. I. Lifshitz, Anomalies of electron characteristics of a metal in the high pressure region. Sov. Phys. J. Exp. Theor. Phys. **11**, 1130 (1960)

Springer

http://www.springer.com/978-3-642-30935-9

Theory of Bilayer Graphene Spectroscopy

Mucha-Kruczyński, M.

2013, X, 86 p., Hardcover

ISBN: 978-3-642-30935-9